Hindawi
Advances in Mathematical Physics
Volume 2023, Article ID 6699888, 18 pages
https://doi.org/10.1155/2023/6699888

Research Article

Implicit Finite Difference Simulation of Hybrid Nanofluid along a Vertical Thin Cylinder with Sinusoidal Wall Heat Flux under the Effects of Magnetic Field

Mashiyat Khan,[1] Amzad Hossain,[1] Afroja Parvin,[1] and Md. Mamun Molla[1,2]

[1]*Department of Mathematics and Physics, North South University, Dhaka-1229, Bangladesh*
[2]*Center for Applied and Computational Science (CACS), North South University, Dhaka-1229, Bangladesh*

Correspondence should be addressed to Md. Mamun Molla; mamun.molla@northsouth.edu

Received 6 August 2023; Revised 23 November 2023; Accepted 24 November 2023; Published 22 December 2023

Academic Editor: Mahnoor Sarfraz

A numerical analysis of magnetohydrodynamic natural convection along a thin vertical cylinder with a sinusoidal heat flux at the wall immersed in copper (Cu) and aluminum-oxide (Al_2O_3) hybrid nanofluids has been studied. A 2D vertical thin cylinder shape geometry has been considered with a radius of R. The fluid flow is considered laminar and incompressible with the Prandtl number of $Pr = 6.2$ and 10% concentration of hybrid nanoparticles. The nondimensional governing equations have been solved numerically by using the implicit finite difference method. An in-house FORTRAN 90 code is used for solving this problem and the code is validated with the available benchmark results. Numerical simulations have been performed for a wide range of governing parameters, Hartmann number from $Ha = 0$ to $Ha = 4$, nanoparticles volume fractions $\phi = 0.0$ to $\phi = 0.1$, and the amplitude of the wall heat flux $\varepsilon = 0.0$–0.3. The findings have been illustrated in terms of streamlines, isotherms, local skin friction coefficients, local Nusselt numbers, velocity, and temperature distributions. The flow field and temperature distribution within the boundary layer are deceased by the effects of the wall heat flux amplitudes. It is also noted that the rate of heat transfer increases with particle volume fraction and the amplitude of the wall heat flux. According to the findings, Nu increases by 24.72% as ϕ increases from 0 to 0.1 while $\varepsilon = 0.3$, and 27.66% while ε increases from 0.0 to 0.3 at 5% hybrid nanoparticles. The local skin frictions and Nusselt number diminish with the increment of the Hartman number due to the effects of the Lorenz force. The findings of this study can lead to a better understanding of the fundamental principles regarding the behavior of hybrid nanofluids under complex conditions, such as a vertical thin cylinder with a sinusoidal wall heat flux. Understanding the behavior of hybrid nanofluids in the presence of a magnetic field and a nonuniform wall heat flow can also lead to the development of innovative heat transfer enhancement strategies.

1. Introduction

The impact of the heating and cooling mechanism on many businesses and consumer goods motivates researchers throughout the world to concentrate on heat transfer studies. Its significance is seen in various industrial processes, including laser cooling, environmental engineering, and thermal power stations. In every engineering application, maximum heat transfer efficiency in the shortest amount of time is preferred. This may be accomplished by using a working fluid with high thermal conductivity. Conventional working fluid options do not meet today's industrial standards because of their poor thermal conductivity. Nanofluid can variously solve this issue. The mixer of the nanofluid is even more thermally conductive than nanofluid, which is defined as a hybrid nanofluid [1]. A hybrid nanofluid on a vertical narrow cylinder experiences natural convective heat transfer in which heat is transferred from the cylinder to the fluid due to buoyancy pressures brought on by variations in temperature. A mixer of nanofluid combines two or more different kinds of nanoparticles that can improve the fluid's thermal characteristics. The transmission phenomena grow more complicated in the presence of the nanofluid/hybrid nanofluid and magnetic field, and they exhibit reliance on the imposed boundary conditions, geometric configuration, and so on [2, 3]. Because of the higher thermal conductivity,

the study of nanofluid and hybrid nanofluid along a vertical wavy surface under different conditions has become popular nowadays [4]. It has many potential applications, such as drug delivery, heat exchanger design, cooling, energy generation, etc. [5].

Numerous types of nanoparticles are introduced into the base liquids to improve the thermal conductivity of a particular fluid, such as water, ethylene glycol, and engine oils. Many studies have been conducted using hybrid nanofluid. Tlili et al. [6] investigate the movement and transmission of energy of (Ti−Cu) based hybrid nanofluid caused by the continuously significant point in the hydromagnetic flow. Arifin et al. [7] looked at the movement of 3D hybrid nano liquids with a particular goal of similarity factors. Giwa et al. [8] discussed mixed nanoliquids with a specific class of nanofluids known for their improved heat and flow properties against single-particle nanoparticles. According to Anitha et al. [9], producing dual-tube heat transfer using a hybrid nanofluid as a cooling system with outer magnetization field effects revealed thermal transport efficacy. In the presence of a hybrid nanofluid and heat radiation, Venkateswarlu et al. [10] watched significant characteristics of varying thermoconduction and viscosity distribution by permeable growing surface. The ratio of the thermal efficiency in a hybrid nanofluid of ethylene glycol and various volume fraction distributions of ethanol glycol as the base liquid was meticulously addressed by Pourrajab et al. [11]. A hybrid nanoliquid's movement and heat transfer were examined by Yashkun et al. [12] in their paper using an exponentially stretched/shrunk surface along with combined convective and Joule heating. All of them have been reported the improved thermal conductivity than ordinary nanofluid. In this context, the present literature review explores the research landscape related to the implicit finite difference simulation of hybrid nanofluids flowing along a vertical thin cylinder exposed to a sinusoidal wall heat flux and subjected to the influence of a magnetic field.

In numerical analysis, the best method for addressing an issue must be chosen based on its benefits and effectiveness. The implicit finite difference approach is a strong, dependable, numerically efficient, and unconditionally convergent way to solve a boundary layer problem in second-order spatiotemporal [13, 14]. Moreover, the implicit finite difference techniques' convenience of use and computational effectiveness have made them popular for modeling heat transport processes. High-performance computing on fluid flow equations using heterogeneous clusters is another capability. Working with unknown functions and their corresponding derivatives at each node simultaneously is necessary for some parts of the complex grid. By using the Keller box approach and, if necessary, defining interface and boundary conditions, this procedure may be made more numerically simple [14]. Many studies have been conducted to provide a comprehensive overview of finite difference methods in heat transfer simulations (see [14–16]).

Natural convection is commonly considered in the numerical research of physical sciences in heat transfer applications. Natural thermal flow (free convection) is a type of mass and heat transmission in which fluid motion is driven by density differences in the fluid induced by temperature gradients rather than by any external device. There are several applications for natural convective flow. Many industrial uses rely on it. It is employed for the convection flow of nanoparticles. Natural magnetohydrodynamic (MHD) convection, classified as convective heat transfer caused solely by the temperature difference of a conductive medium in the magnetic field, has gained a lot of interest [17, 18] in various studies, including boundary layer problems [19]. Very few studies have been performed to analyze the effect of free convection along a vertical cylinder. Studies of fluid flow about a cylinder are usually 2D since the radius is taken into account more thoroughly than boundary layer thickness. Processing equipment operating at low pressure often uses thin cylinders or any thin-walled shapes. It is worthwhile to highlight a few of the earlier free convective studies conducted by researchers on cones or cylinders. In a thermally stratified medium, Hossain et al. [20] investigated natural convection over a vertical circular cone having uniform surface heat flux and temperature; nevertheless, further in-depth talks on different fluids or Prandtl numbers (Pr) are still needed. Hossain and Alim [21] considered the impact of radiation on a thin vertical cylinder's boundary layer for fixed Pr; however, their results were restricted to the surface temperature uniformity. Gori et al. [13] provided a much better presentation since they showed the applicability of their method with both high ($Pr = 730$) and low ($Pr = 0.7$) Pr. Nonetheless, further consideration was needed for the viscosity variations. Pr can also reveal the sort of fluids in a standard numerical study by connecting viscosity and thermal conductivity. According to Smith et al. [22], a larger Pr (>5) denotes heat transfer that is influenced by fluid momentum as opposed to thermal diffusion. As a result, adopting a numerical strategy to the relevant sector is more confidently established when Pr varies at different scales. Most of the time, the existing literature lacks a thorough examination that integrates hybrid nanofluids, sinusoidal wall heat flux, magnetic field effects, and implicit finite difference simulations on a vertical thin cylinder, despite the notable advancements in each of these domains. To improve our comprehension of intricate heat transfer processes and enhance thermal system design, this review emphasizes the necessity of conducting a thorough investigation that unites various ideas.

The objective of this study stems from the fact that this sort of boundary condition occurs frequently in practice. As a result, based on the aforementioned literature, it is evident that more excellent research into the MHD-free convection combined with the hybrid nanofluid in a thin vertical cylinder is required. The present study aims to analyze numerical simulations of MHD natural convection of hybrid nanofluid in a thin vertical cylinder. The findings of this study can lead to a better understanding of the fundamental principles regarding the behavior of hybrid nanofluids under complex conditions, such as a vertical thin cylinder with a sinusoidal wall heat flux. Understanding the behavior of hybrid nanofluids in the presence of a magnetic field and a nonuniform wall heat flow can also lead to the development of innovative heat transfer enhancement strategies.

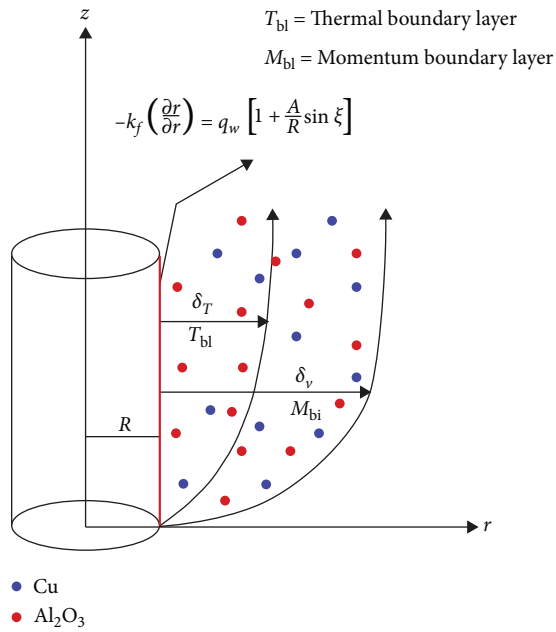

Figure 1: Schematic diagram of the vertical thin cylinder with the coordinate system.

Table 1: Properties of the nanoparticles and base fluid (H_2O, Cu, and Al_2O_3).

Elements name	Density ρ (kg m^{-3})	Specific heat at constant pressure C_p (J kg K^{-1})	Thermal conductivity k (W m^{-1} K)	Electric conductivity σ (S m^{-1})	Thermal expansion coefficients (β) (K^{-1})
Pure water (H_2O)	991.1	4,179	0.613	0.05	
Copper (Cu)	8,933	385	401	5.96×10^{7}	1.67×10^{-5}
Alumina (Al_2O_3)	3,970	765	40	3.69×10^{7}	0.85×10^{-5}

2. Theoretical Formulation

2.1. Problem Statement. A 2D vertical thin cylinder of radius R with nonuniform heat flux $-k_f(\frac{\partial T}{\partial r}) = -q_w[1+\frac{A}{R}\sin\xi]$ is considered, as shown in Figure 1. The fluid flow is considered laminar and incompressible with the Prandtl number of $Pr = 6.2$, and the cylinder is immersed in a mixture of water with Cu and Al_2O_3 hybrid nanoparticles. Both are considered to be in the fluid phase, with nanoparticles in thermodynamic equilibrium and moving at the same velocity.

2.2. Hybrid Nanofluid. Nanofluids are nanoparticles used as a passive control parameter in various energy systems, including solar power, heat exchanger design, and cooling processes. Hybrid nanofluids are constructed to directly mix up two different nanoparticles with a base fluid. In this work, it is considered that the Cu/Al_2O_3-water hybrid nanofluids improve their thermal performance, such as conductivity, heat transfer, and other fundamental features. The thermophysical properties of the nanoparticles and based fluid are given in Table 1.

The effective density ρ_{hnf} and dynamic viscosity μ_{hnf} of nanofluids can be stated as follows [17]:

$$\rho_{hnf} = (1-\phi)\rho_f + \phi\rho_{np}, \tag{1}$$

where ϕ is the particle volume fraction, subscripts f and s represent the base fluid and solid particle, respectively, and [10, 17]

$$\mu_{hnf} = \frac{\mu_f}{(1-\phi)^{2.5}}. \tag{2}$$

Therefore, the thermal diffusivity α_{hnf} is as follows [4, 5, 17]:

$$\alpha_{hnf} = \frac{k_{hnf}}{(\rho C_p)_{hnf}}, \tag{3}$$

where the thermophysical characteristics of hybrid nanofluid are as follows [5, 17]:

$$k_{hnf} = \frac{k_{np} + 2k_f - 2(k_f - k_{np})\phi}{k_{np} + 2k_f + (k_f - k_{np})\phi}k_f, \tag{4}$$

$$(\rho C_p)_{hnf} = (1-\phi)(\rho C_p)_f + \phi(\rho C_p)_{np}, \tag{5}$$

$$(\rho\beta)_{hnf} = (1-\phi)(\rho\beta)_f + \phi(\rho\beta)_{np}. \tag{6}$$

That is, $np1 = Al_2O_3$ and $np2 = Cu$

$$\phi = \phi_{np1} + \phi_{np2}, \tag{7}$$

$$k_{np} = \frac{\phi_{np1}k_{np1} + \phi_{np2}k_{np2}}{\phi}, \tag{8}$$

$$\rho_{np} = \frac{\phi_{np1}\rho_{np1} + \phi_{np2}\rho_{np2}}{\phi}, \tag{9}$$

$$\left(C_p\right)_{np} = \frac{\phi_{np1}\left(C_p\right)_{np1} + \phi_{np2}\left(C_p\right)_{np2}}{\phi}, \tag{10}$$

$$\beta_{np} = \frac{\phi_{np1}\beta_{np1} + \phi_{np2}\beta_{np2}}{\phi}. \tag{11}$$

The electrical conductivity for hybrid nanofluid is as follows [4, 5, 10, 17]:

$$\sigma_{hnp} = \sigma_f\left[1 + \frac{3\left(\frac{\sigma_{np}}{\sigma_f} - 1\right)\phi}{\left(\frac{\sigma_{np}}{\sigma_f} + 2\right) - \left(\frac{\sigma_{np}}{\sigma_f} - 1\right)\phi}\right], \tag{12}$$

where

$$\sigma_{np} = \frac{\phi_{np1}\sigma_{np1} + \phi_{np2}\sigma_{np2}}{\phi}, \tag{13}$$

where $np1$ and $np2$ stand for nanoparticle 1 and nanoparticle 2, respectively.

The properties of the water (H_2O), copper (Cu), and alumina (Al_2O_3) particles are given below [4, 5, 10, 17]:

2.3. Governing Equations. The governing equation for the boundary layer in cylindrical coordinates is considered as in [23–26]:

$$\frac{\partial}{\partial x}(rx) + \frac{\partial}{\partial y}(ry) = 0, \tag{14}$$

$$\rho_{hnf}\left(u\frac{\partial u}{\partial x} + v\frac{\partial u}{\partial r}\right) = \frac{\mu_{hnf}}{r}\frac{\partial}{\partial r}\left(r\frac{\partial u}{\partial r}\right) + g(\rho\beta)_{hnf}(T - T_\infty) - \sigma_{hnf}B_o^2 u, \tag{15}$$

$$u\frac{\partial T}{\partial x} + v\frac{\partial T}{\partial y} = \frac{\alpha_{hnf}}{r}\frac{\partial}{\partial r}\left(r\frac{\partial T}{\partial r}\right), \tag{16}$$

where x-coordinates are along the axis, and r-coordinates are perpendicular to the x-axis, u and v velocity components are along x and r directions, respectively. Here, B_0 is the magnetic field strength, and g is the acceleration due to gravity.

The corresponding boundary conditions [27] are as follows:

$$u = v = 0, -k_f\frac{\partial T}{\partial r} = q_w\left[1 + \frac{A}{R}\sin\xi\right] \text{at}, r = 0, \tag{17}$$

$$u \to 0, v \to 0, T \to T_\infty, r \to \infty. \tag{18}$$

For the local nonsimilarity solutions, the nondimensional variables are defined as follows [4, 5, 17]:

$$\xi = \frac{2x}{R}Gr_x^{-1/5},\ \ \eta = \frac{r^2 - R^2}{2Rx}Gr_x^{1/5},\ \ \frac{r^2}{R^2} = 1 + \xi\eta,$$
$$\psi = 5\nu_f RGr_x^{1/5}f(\xi,\eta), \tag{19}$$

$$\theta = \frac{T - T_\infty}{\left(\frac{q_w x}{k_f}\right)}Gr_x^{1/5},\ Gr = \frac{g\beta_f q_w x^4}{5k_f\nu_f^2},\ Ha = \sqrt{\frac{\sigma_f}{\mu_f}}B_o R. \tag{20}$$

Here, Gr is the Grashof number, Ha is the Hartmann number, θ is the nondimensional temperature, k_f is the thermal conductivity, σ_f is the electric conductivity, and μ_f is the dynamics viscosity of the base fluid.

The nondimensional velocity components can be calculated from the stream function as follows:

$$u = \frac{1}{r}\frac{\partial\psi}{\partial r},\quad v = \frac{1}{r}\frac{\partial\psi}{\partial x} \tag{21}$$

where

$$v = -\frac{R}{r}\frac{\nu_f}{x}Gr_x^{1/5}\left[\xi\frac{\partial f}{\partial\xi} - \eta f' + 4f\right], u = 5\frac{\nu_f}{x}Gr_x^{2/5}f', \tag{22}$$

$$\frac{\partial u}{\partial x} = \frac{\nu_f}{x}Gr_x^{2/5}\left[\xi\frac{\partial f'}{\partial\xi} - \eta f'' + 3f'\right], \tag{23}$$

$$\frac{\partial u}{\partial r} = \left(\frac{r}{R}\right)5\frac{\nu_f}{x^2}Gr_x^{3/5}f'', \tag{24}$$

$$\frac{\partial}{\partial r}\left(r\frac{\partial T}{\partial r}\right) = \left(\frac{r^3}{R^2}\right)5\frac{\nu_f}{x^3}Gr_x^{4/5}f''' + \left(\frac{r}{R}\right)5\frac{\nu_f}{x^2}Gr_x^{3/5}f'' + \left(\frac{r}{R}\right)5\frac{\nu_f}{x^2}Gr_x^{3/5}f''. \tag{25}$$

Here, by putting values of Equations (22)–(25) in Equation (15), we get the final form of the momentum equation as follows:

$$\frac{\rho_{hnf}}{\rho_f}\frac{\mu_{hnf}}{\mu_f}[(1+\xi\eta)f''' + \xi f''] + 4ff'' - 3f'^2 + \frac{\beta_{hnf}}{\beta_f}\theta - \frac{\sigma_{hnf}\rho_f}{\sigma_f\rho_{hnf}}Ha^2\xi^2 f' = \xi\left(f'\frac{\partial f'}{\partial \xi} - f''\frac{\partial f}{\partial \xi}\right). \tag{26}$$

For the energy equations, the following calculations are as follows:

$$\frac{\partial T}{\partial x} = \frac{q_w}{5k_f Gr_x^{1/5}}\left[\xi\frac{\partial \theta}{\partial \xi} - \eta\theta + \theta\right], \tag{27}$$

$$\frac{\partial u}{\partial r} = \left(\frac{r}{R}\right)\frac{q_w}{k_f}\theta', \tag{28}$$

$$\frac{\partial}{\partial r}\left(r\frac{\partial T}{\partial r}\right) = \left(\frac{r^3}{R^2}\right)\frac{q_w}{k_f x}Gr_x^{1/5}\theta'' + 2\left(\frac{r^3}{R^2}\right)\frac{q_w}{k_f}\theta'. \tag{29}$$

From Equations (27)–(29), we get the final result for temperature. That is:

$$\frac{1}{Pr}\frac{\alpha_{hnf}}{\alpha_f}[(1+\xi\eta)\theta'' + \xi\theta'] + 4\theta' f - \theta f' = \xi\left[f'\frac{\partial \theta}{\partial \xi} - \theta'\frac{\partial f}{\partial \xi}\right]. \tag{30}$$

The corresponding boundary conditions are as follows:

$$f = f' = 0, \theta' = -[1 + \varepsilon\sin(\pi\xi)] \text{ at, } \eta = 0, \tag{31}$$

$$f = \theta = 0, \text{ as, } \eta \to \infty, \tag{32}$$

where $\varepsilon = AR$ is the amplitude of the non-uniform heat flux and $Pr = \nu_f/\alpha_f$ is the Prandtl number. The detailed calculation of the above derivatives is given in Appendix.

3. Numerical Methods

Now, the local nonsimilar boundary layer Equations (26) and (30) will be transformed into a suitable form for the implicit finite difference method.

Let $f = V$ and $U = f'$ consequently $\frac{\partial U}{\partial \eta} = f''$ and $\frac{\partial^2 U}{\partial \eta^2} = f'''$ then Equation (26) becomes:

$$N_1\frac{\partial^2 U}{\partial \eta^2} + N_2\frac{\partial U}{\partial \eta} + 4V\frac{\partial U}{\partial \eta} - 3U^2 + N_3\theta - N_4 U = \xi\left(U\frac{\partial^2 U}{\partial \xi} - \frac{\partial U}{\partial \eta}\frac{\partial V}{\partial \xi}\right). \tag{33}$$

Equation (33) is discretized by the finite difference method, where the diffusion and convection terms are by major difference. The ξ-derivative term is discretized by the different backward formulas for numerical stability. The following results in the creation of a system of algebraic equations:

$$A_{i,j}F_{i,j-1} + B_{i,j}F_{i,j} + C_{i,j}F_{i,j+1} = D_{i,j}. \tag{34}$$

For the transformed momentum Equation (33), the matrix coefficients are as follows:

$$A_{i,j} = \left(N_1 - T_1\frac{\Delta\eta}{2}\right), \tag{35}$$

$$B_{i,j} = -2N_1 + \left(-3U_{i,j} - N_4\right)\Delta\eta^2 - \xi U_{i,j}\frac{\Delta\eta^2}{\Delta\xi}, \tag{36}$$

$$C_{i,j} = \left(N_1 + T_1\frac{\Delta\eta}{2}\right), \tag{37}$$

$$D_{i,j} = -N_3\theta_{i,j}\Delta\eta^2 - \xi U_{i,j}U_{i-1,j}\frac{\Delta\eta^2}{\Delta\xi}, \tag{38}$$

where

$$N_1 = \frac{\mu_{hnf}\rho_f}{\mu_f\rho_{hnf}}(1+\xi\eta), \quad N_2 = \frac{\mu_{hnf}\rho_f}{\mu_f\rho_{hnf}}\xi, \quad N_3 = \frac{\beta_{hnf}}{\beta_f}, \quad N_4 = \frac{\sigma_{hnf}}{\sigma_f}\frac{\rho_f}{\rho_{hnf}}Ha^2\xi^2 \text{ and } T_1 = 4V_{i,j} + N_2 + \xi\frac{\partial V}{\partial \xi}. \tag{39}$$

Similarly, for the energy Equation (30), the matrix coefficients are as follows:

$$A_{i,j} = \left(N_1 - T_1\frac{\Delta\eta}{2}\right), \tag{40}$$

$$B_{i,j} = -2N_1 - U_{i,j}\Delta\eta^2 - \xi U_{i,j}\frac{\Delta\eta^2}{\Delta\xi}, \tag{41}$$

$$C_{i,j} = \left(N_1 + T_1\frac{\Delta\eta}{2}\right), \tag{42}$$

$$D_{i,j} = -XU_{i,j}\theta_{i-1,j}\frac{\Delta y^2}{\Delta x}, \tag{43}$$

where

$$N_1 = \frac{1}{Pr}\frac{\alpha_{hnf}}{\alpha_f}(1+\xi\eta), \; N_2 = \frac{1}{Pr}\frac{\alpha_{hnf}}{\alpha_f}\xi \text{ and } T_1 = 4V_{i,j} + N_2 + \xi\frac{\partial V}{\partial \xi}, \tag{44}$$

where $F_{i,j}$ is the generic variable for the U-velocity and temperature θ. The algebraic Equation (34) is solved by the Thomson algorithm. In computation, the velocity ($V_{i,j}$) component along the normal direction is attained after solving the equation $U = f' = V'$ as follows:

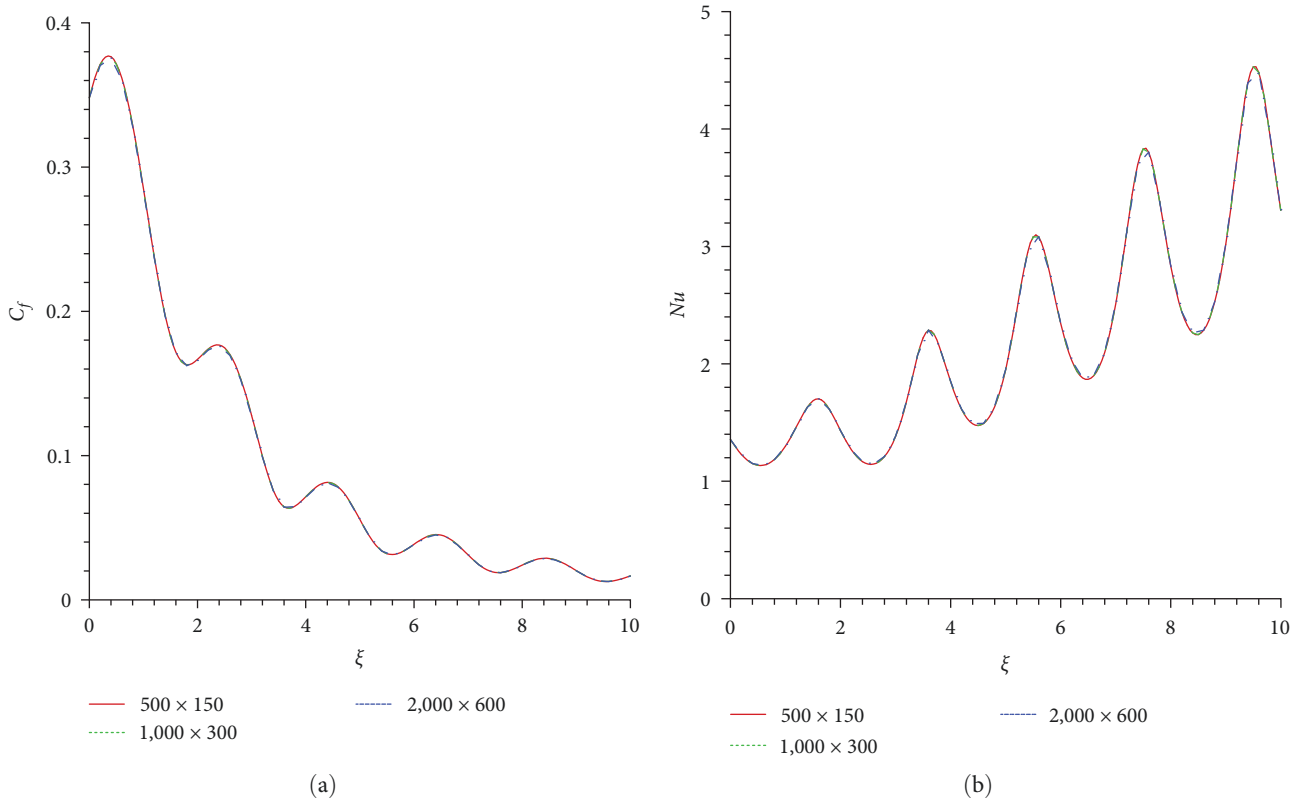

FIGURE 2: Grid independent test for the three different grid sizes ($\xi \times \eta$): (a) local skin-frictions and (b) Russel Nusselt number while case 1—500×150, case 2—$1{,}000 \times 300$, and case 3—$2{,}000 \times 600$, while $Pr = 6.2$, $Ha = 2$, $\varepsilon = 0.3$, and $\phi = 0.1$.

$$V_{i,j} = V_{i,j-1} + \frac{1}{2}\left(U_{i+1,j} + U_{i,j+1}\right)\Delta\eta. \tag{45}$$

From $\xi = 0.0$, the iteration begins and then continues downstream discreetly. The tolerance for the iteration process is 10^{-6}. An in-house FORTRAN 90 code based on the above discretization, a marching order implicit finite difference method (MOIFDM), is used for the present simulation.

4. Local Skin-Friction Coefficient and the Local Nusselt Number

From the numerical solutions of the above equations, two physical quantities are calculated, such as local shearing stress in terms of the local skin friction coefficient C_f, the local rate of heat transfer Nu, and the average rate of heat transfer $\overline{Nu}$. These quantities play an essential role in their physical significance and can be expressed using the following dimensionless relations:

$$C_f\left(5Gr_x^{1/5}\right) = f''(\xi, 0), \tag{46}$$

$$NuGr_x^{-1/5} = \frac{k_{hnf}}{k_f}\frac{1}{\theta(\xi, 0)}. \tag{47}$$

5. Grid-Independent Test and Code Validation

In computational fluid dynamics research, it is an obvious event to study the grid independence test (GIT) and the code validation. The GIT and code validation are shown in the following subsections.

5.1. Grid-Independent Test. Conducting the grid-independent test is a mandatory step for any numerical simulation.

Here, three different grid sizes ($\xi \times \eta$): Case 1—500×150, Case 2—$1{,}000 \times 300$, and Case 3—$2{,}000 \times 600$ have been considered, and the results are shown in Figures 2(a) and 2(b) in terms of the local skin-frictions and Nusselt number, respectively. From Figures 2(a) and 2(b), it is evident that numerical solutions are grid independence.

5.2. Code Validation. Code validation is also an important step of any numerical simulation. The present code is validated for the heat flux boundary condition along a vertical flat and wavy surface investigated by Moulic and Yao [25]. A comparison in terms of the surface temperature (θ_w (ξ, 0)) for a vertical flat plate ($\alpha = 0$) and a wavy surface ($\alpha = 0.1$) is shown in Figure 3. This comparison shows an excellent agreement. Another comparison has been made for a vertical thin cylinder with wall heat flux in terms of the Nusselt

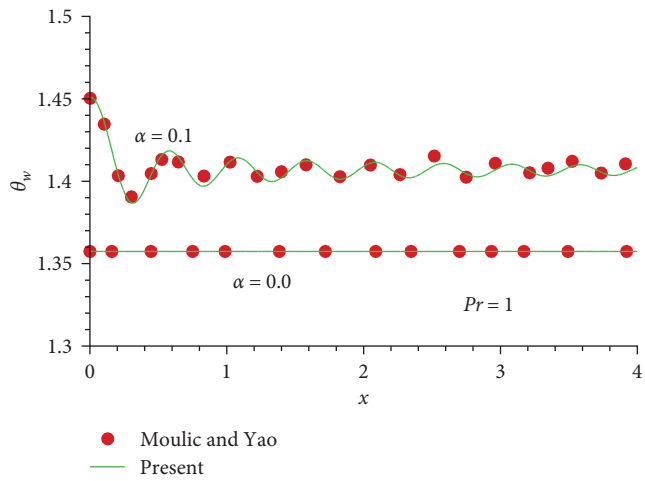

Figure 3: Comparison between present numerical results for the heat flux boundary condition in terms of the surface temperature $\theta_w(\xi, 0)$ of Moulic and Yao [25] while $Pr = 1$ and the surface waviness $\alpha = 0, 0.1$.

Table 2: Comparison of the present results in terms of the Nusselt number with the results of Heckel et al. [26] for a vertical thin cylinder with wall heat flux while $\phi = 0.0$.

ξ	$Nu_x\, Gr_x^{-1/5}$ Heckel et al. [26]				$Nu_x\, Gr_x^{-1/5}$ Present			
	$Pr = 0.1$	$Pr = 0.7$	$Pr = 7.0$	$Pr = 100$	$Pr = 0.1$	$Pr = 0.7$	$Pr = 7.0$	$Pr = 100$
0	0.2634	0.4834	0.8699	1.5560	0.2637	0.4813	0.8711	1.5712
0.5	0.3416	0.5640	0.9533	1.6385	0.3519	0.5484	0.9941	1.6829
1.0	0.5448	0.7820	1.1809	1.8736	0.5651	0.8112	1.2391	1.9261
1.5	0.8691	1.1013	1.5135	2.2352	0.8897	1.1531	1.6013	2.2902
2.0	1.3243	1.5052	1.9828	2.6904	1.3352	1.6135	2.0012	2.7346
2.5	1.8971	2.0068	2.4967	3.2133	1.9279	2.0119	2.5732	3.2715
3.0	2.5789	2.6321	3.0592	3.8831	2.5924	2.8242	3.1321	3.9417
3.5	3.3666	3.3915	3.6970	4.6065	3.4112	3.4551	3.7519	4.6751
4.0	4.2626	4.2757	4.4554	5.4551	4.3132	4.3772	4.5203	5.5115
4.5	5.2756	5.2828	5.3785	6.3389	5.3421	5.3683	5.4133	6.3891
5.0	6.4224	6.4271	6.4791	7.3556	6.5605	6.5915	6.6410	7.4061

number with the results of Heckel et al. [26] by varying the Prandtl number, which is shown in Table 2. From Table 2, it is also evident the present code is suitable for the vertical thin cylinder with wall heat flux condition.

6. Results and Discussions

The present study discussed the Cu and Al_2O_3 hybrid nanofluids along a thin vertical cylinder with uniform heat flux conditions at different parameters such as particle volume fractions, Hartmann numbers, and amplitudes. Based on these parameters, three sets of the results are shown graphically as streamlines and isotherms, temperature and velocity distribution with skin friction, and Nusselt number for the amplitude variations, Hartmann number, and volume fraction.

6.1. Effect of the Amplitude of the Wall Heat Flux. Figure 4 shows the effects of the amplitude of sinusoidal temperature (ε) on the nondimensional velocity and temperature inside the fluid flow. The velocity in the x-direction is plotted against the height of the cylinder in the mid-section along the vertical direction, as shown in Figure 4 for amplitude. Figure 4 indicates the u-velocity and the temperature distribution of a thin vertical cylinder for nanoparticle amplitudes from $\varepsilon = 0.0$ to 0.3. In fluid flow, the velocity and temperature can be significantly impacted by ε. The rise in the ε can change the fluid's density, reducing the fluid flow and affecting the spread of temperature. As seen from the figure, the velocity and temperature distribution variation exhibit similar trends at the beginning and end but vary when the temperature $\theta = 0.06$–$\theta = 0.09$. The fluids inside the boundary layer drop their velocity, and the temperature when ε gradually increases. The fluids in the boundary layer move at the minimum velocity when the surface temperature is low. The velocity decreases as the amplitude increases. Temperature variations of greater amplitude reduce the more vigorous

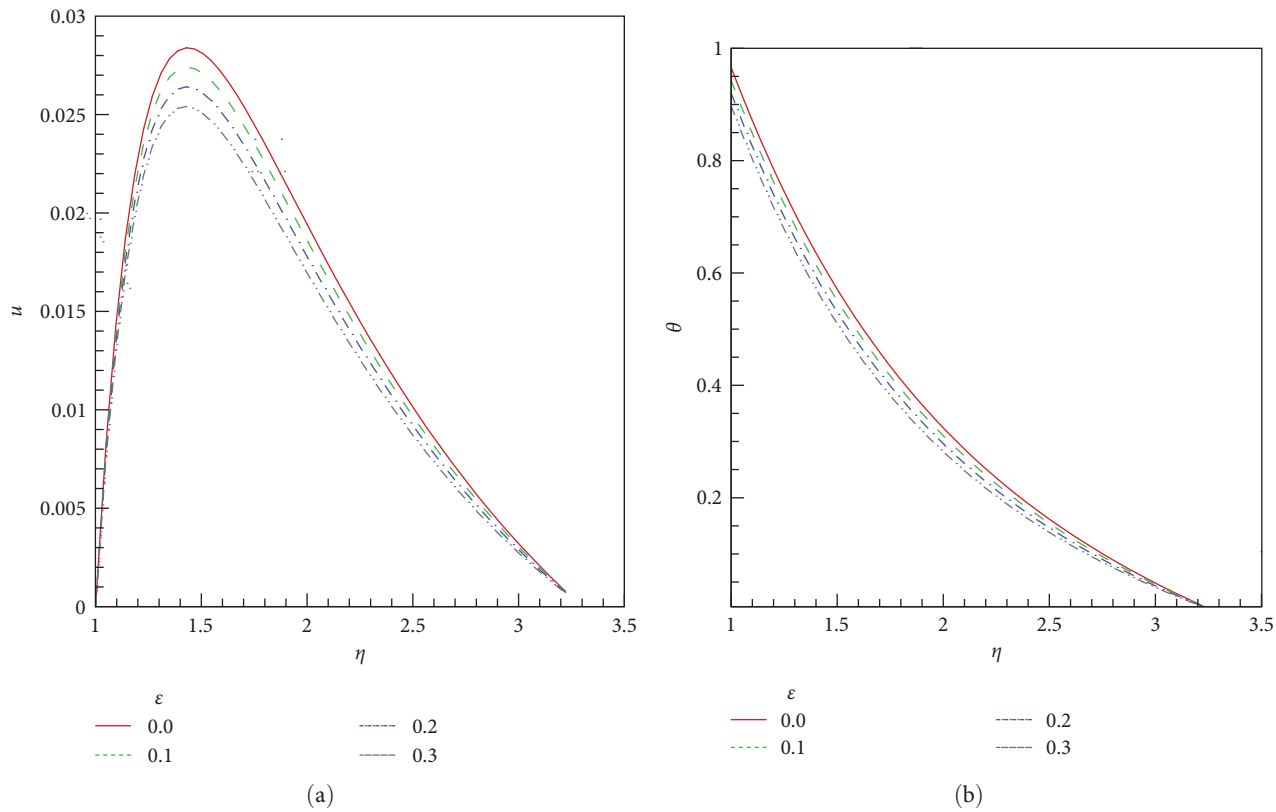

FIGURE 4: (a) Velocity and (b) temperature with different amplitude, for $\varepsilon = 0.0$, $\varepsilon = 0.1$, $\varepsilon = 0.2$, and $\varepsilon = 0.3$, while $\phi = 0.05$ and $Ha = 2$.

fluid motion, resulting in a drop in velocity. Another impact of raising the amplitude is a shift in temperature distribution when the amplitude is raised, resulting in a lower spread of temperature.

In skin friction C_f and Nusselt number Nu, we can see that when skin friction increases due to the increasing amplitude. The Nusselt number increases with the increase of the volume fraction. That is, the channel geometry and the boundary condition on the wall heat transfer determine the Nusselt number in a fully developed laminar flow, which is constant. The effects of skin friction (C_f) and Nusselt number (Nu) on the flow fields of the thin vertical cylinder for different amplitudes of the vertical thin cylinder (ε) are illustrated in Figure 5. C_f and Nu in fluid dynamics can be influenced by ε. Nu is a dimensionless number employed to characterize the heat transmission between a fluid and a solid surface, whereas C_f refers to the shear stress between a fluid and a solid surface.

As the larger amplitude of sinusoidal temperature flows tends to produce more substantial shearing pressures between the fluid and the surface, doing so can generally increase C_f. Moreover, the amplitude of the vertical thin cylinder can influence the amplitude of the velocity oscillations, which can affect the C_f of the variations in amplitude. This is because changes in fluid viscosity brought on by temperature changes can result in buoyancy pressures that propel fluid motion. More significant buoyancy pressures and more ferocious fluid movement can result from temperature changes of higher magnitude, which can increase C_f. From Figure 5(a), it is evident from the graph that raising the ε of the fluid flow can result in higher amounts of heat transmission, which leads to an increase in C_f and Nu. Initially, at $\varepsilon = 0$, the C_f and Nu distribution was flat; with the increase in ε, the amplitude of the C_f and Nu also increased. Furthermore, adding hybrid nanoparticles to a conventional fluid increases its heat capacity and thermal conductivity, increasing the C_f and Nu [27]. Convective heat transmission between the fluid and the surface can rise if the temperature fluctuation's amplitude increases. This is because temperature changes may result in more significant convective currents and improved heat transmission. That is why the Nu can increase with an increase in the ε, which is evident from Figure 5(b).

The effect of amplitude $\varepsilon = 0.0$–$\varepsilon = 0.3$ on the flow pattern with streamline and isotherms with $Ha = 2$ have been presented in Figure 6 while $\phi = 0.0$ (solid lines) and $\phi = 0.1$ (dashed lines). It shows that the magnitude of the streamline and isotherm increases with sinusoidal temperature amplitude. For different amplitudes, the streamlines and isotherm vary; that is, the waves increase as we increase the amplitudes from 0.0 to 0.3. The waviness of the flow pattern also increases as ε increases. The highest magnitude of stream function has been found with a rise in nanoparticles. Adding 10% of hybrid nanoparticles increases the thermal conductivity of the fluid. Hence, the magnitude of the stream function is improved. Compared to the isotherm of simple fluid, the isotherms of nanofluids lean toward the left wall. When

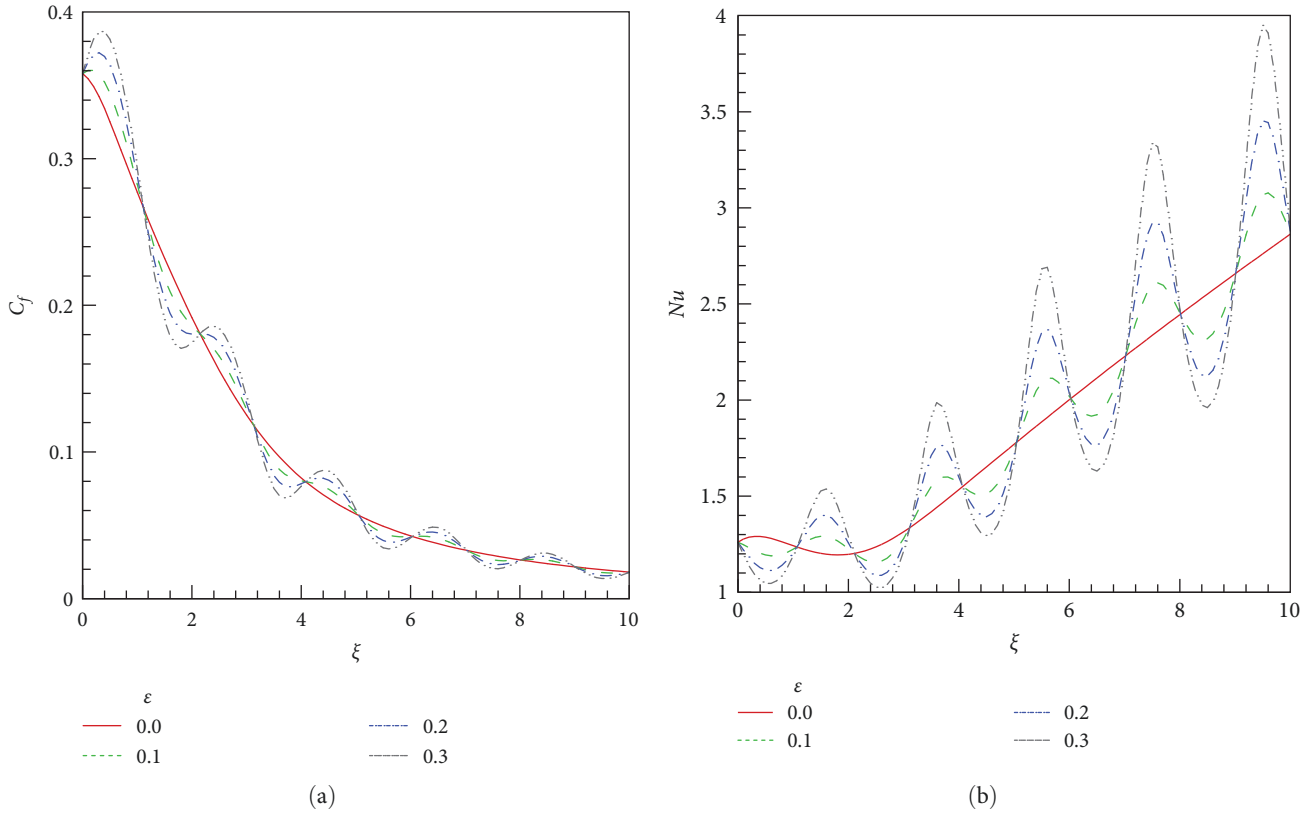

FIGURE 5: (a) Skin friction and (b) Nusselt number with different amplitude for $\varepsilon = 0.0$, 0.1, 0.2, and 0.3; while $\phi = 0.05$ and $Ha = 2$ at $\xi = 2$.

the value grows, it is seen that both the thermal and momentum boundary layers grow. As a result, nanoparticles have little impact at the border layer, and their impact progressively grows as the fluid inside the enclosure moves.

6.2. Effect of Hartmann Number. The intensity of the magnetic field in a fluid flow is expressed by the dimensionless Hartmann number (Ha). In the event of a magnetic field, the Ha significantly affects a conducting fluid's velocity and temperature fields. The fluid's velocity diminishes as the Ha number rises due to the flow's greater magnetic damping. Due to the more substantial magnetic damping experienced by high-conductivity fluids, this impact is more evident. In a conductive fluid, the temperature spread is also impacted by the Ha number. Due to the magnetic field's effect, the temperature profile generally improves with rising Ha. In Figure 7(b), the temperature distribution for the Ha number increases as the Ha increases. The temperature rises when the Ha number increases in magnitude. The velocity distribution begins at a minimum at the wall, peaks near the heated wall, and then declines to zero. It is evident that as Ha grows, it takes longer to attain the temporal maximum velocity. It is observed that when Ha increases, the magnitude of the peak velocity decreases. In summary, when the Hartmann number rises, the strong magnetic field restricts fluid motion, resulting in lower velocity. The drop in kinetic energy caused by the decrease in velocity is compensated for by an increase in internal energy, resulting in a greater temperature.

Figure 8 represents the local and average heat transfer rates in terms of Nusselt numbers along the hot wall. Skin friction and Nusselt number indicate the magnitude of convectional heat transfer. It is noted that the local heat transfer rate increases with particle volume fractions. For which the plot shows a single graph line. Here, the Hartmann number is from $Ha = 1$ to $Ha = 2$. The skin friction is practically parallel to the independent axis, corresponding to the lowest value of the number, $Ha = 0$. With an increase in surface temperature, the Nusselt number similarly rises in value. With an increase in the curvature parameter, the Nusselt number similarly rises in value. In summary, when the Hartmann number grows, skin friction decreases because magnetic forces become more prominent, resulting in the establishment of laminar flow and a reduction in the chaotic motion of the fluid. This reduces skin friction at the limits of the conducting fluid.

In Figure 9, we have seen the streamline and isotherm for different Hartmann numbers and volume fractions. Here, we took the data for the Hartmann number from $Ha = 0$ to $Ha = 4$. But in the plotting, we plotted for the streamline and isotherm of the $Ha = 0$, $Ha = 2$, and $Ha = 4$ with volume fraction $\phi = 0.0$ and $\phi = 0.1$. It has been observed that when the Hartmann number grows, the magnetic field's impact on both streamlines and isotherms becomes more significant. Following the magnetic field lines, streamlines become more organized and laminar. At large Ha numbers, isotherms become substantially elongated along the magnetic

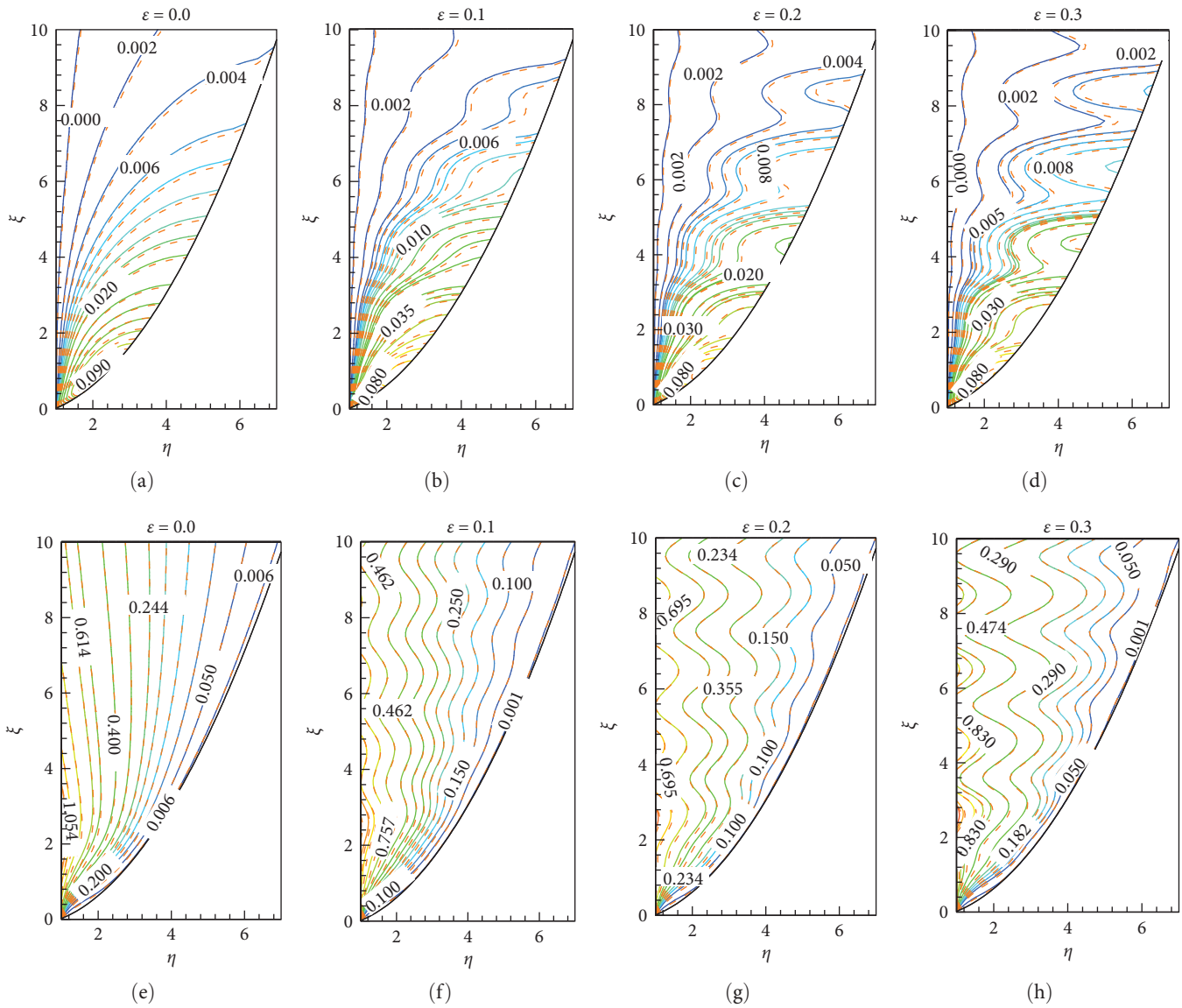

Figure 6: Streamline (top) and isotherm (bottom) for different amplitudes (a), (e) $\varepsilon = 0.0$; (b), (f) $\varepsilon = 0.1$; (c), (g) $\varepsilon = 0.2$, and (d), (h) $\varepsilon = 0.3$; while $\phi = 0.0$ (solid lines) and $\phi = 0.1$ (dashed lines) with $Ha = 2$.

field direction, reflecting the anisotropic character of heat transport in MHD processes. Due to streamwise variations in the surface temperature, the fluid flow may oscillate close to the boundary line [28]. Isotherms tend to be quite homogeneous and do not display considerable temperature changes in the absence of strong magnetic forces ($Ha = 0$). Heat transmission is principally controlled by conduction and convection. Magnetic influences on temperature distribution become more prominent with large Hartmann numbers ($Ha = 4$). Isotherms become extremely stretched along the magnetic field lines. The substantial inhibition of fluid velocity perpendicular to the magnetic field causes this elongation.

In Figure 10, it can be shown that as the parameter increases, the volume fraction distribution of temperature and nanoparticles rise while those of velocity within the boundary layer decline. In Figure 10, the velocity decreases at the beginning due to a certain amount of temperature, and the viscosity is higher in the beginning. The volume fraction's velocity increases, and the fluid's viscosity decreases as the temperature increases. However, the average heat transfer rate increases slowly with volume fractions but increases significantly with increasing Nusselt's number. Similar results have been found by Chamkha et al. [29], which stated that adding nanoparticles to the fluid enhances the velocity, temperature, and skin friction, as well as the rate of heat transfer. It is observed that the velocity profiles begin at zero at the wall, reach their maximum at the hot wall, and then monotonically drop to zero. It is evident that as Ha grows, so does the time required to attain the temporal maximum of velocity. It is seen that the magnitude of the peak velocity decreases as Ha increases. It is evident from the preceding explanation that ignoring the temperature-dependent fluctuation of Ha creates a significant mistake.

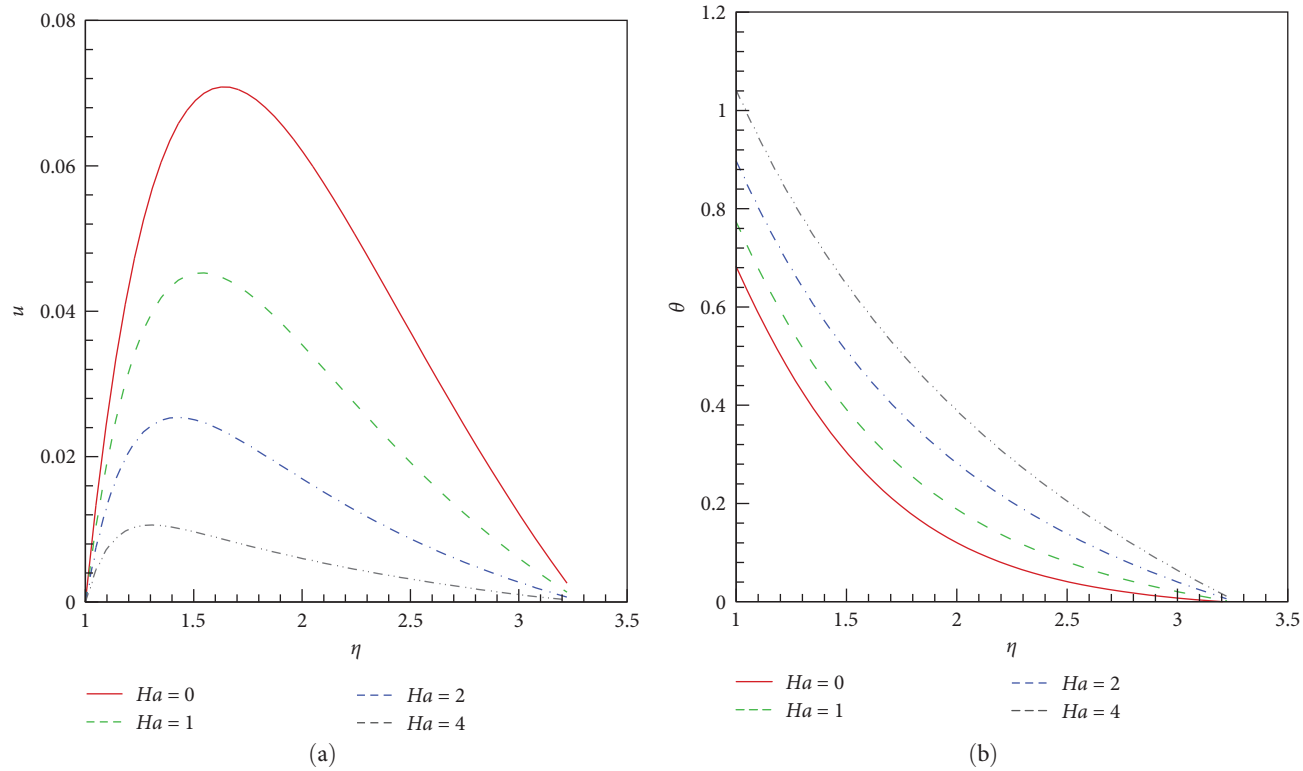

FIGURE 7: (a) Velocity and (b) temperature with different Hartmann numbers, while $\varepsilon = 0.3$, $\phi = 0.05$, $Pr = 6.2$ at $\xi = 2$.

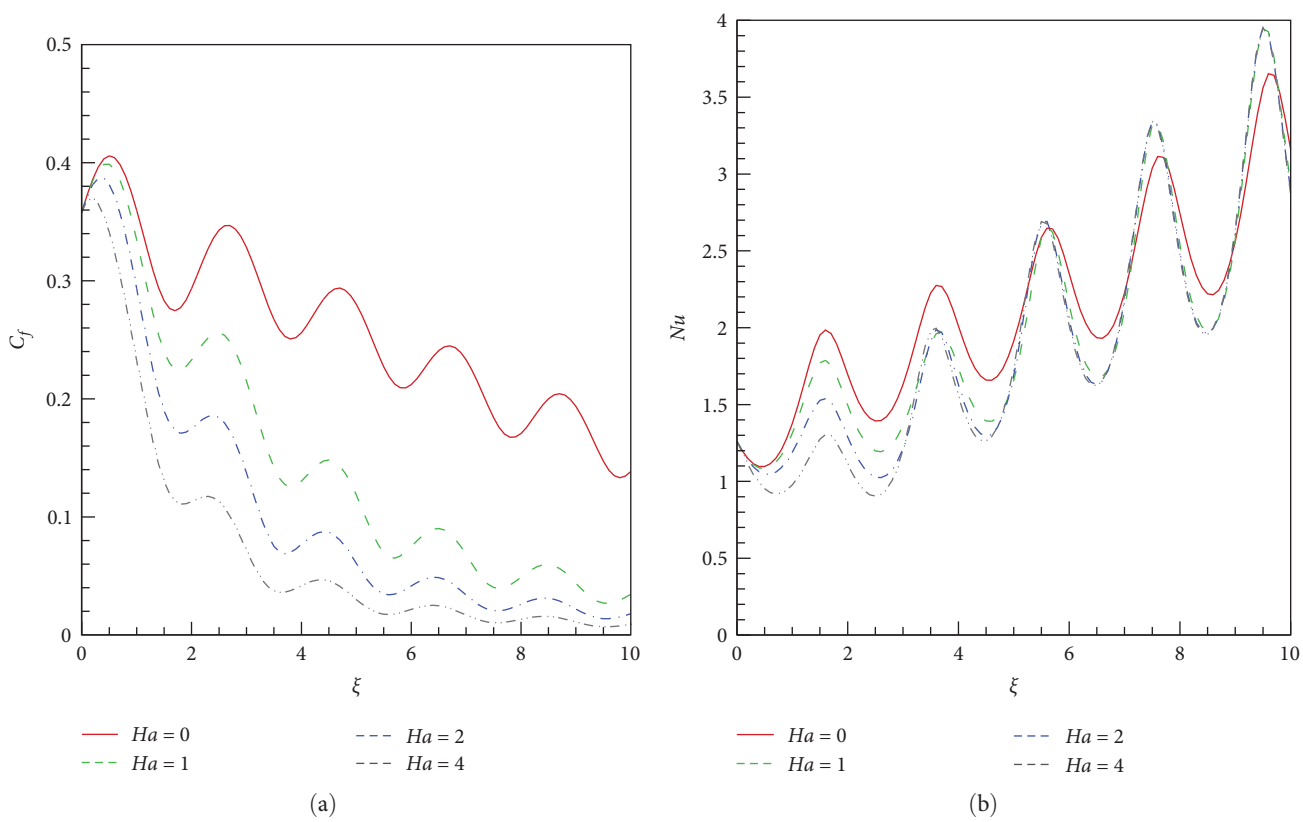

FIGURE 8: (a) Skin friction and (b) Nusselt number with different Hartmann numbers, for $Ha = 1$, $Ha = 2$, and $Ha = 4$; while $\varepsilon = 0.3$ and $\phi = 0.05$ with $Pr = 6.2$.

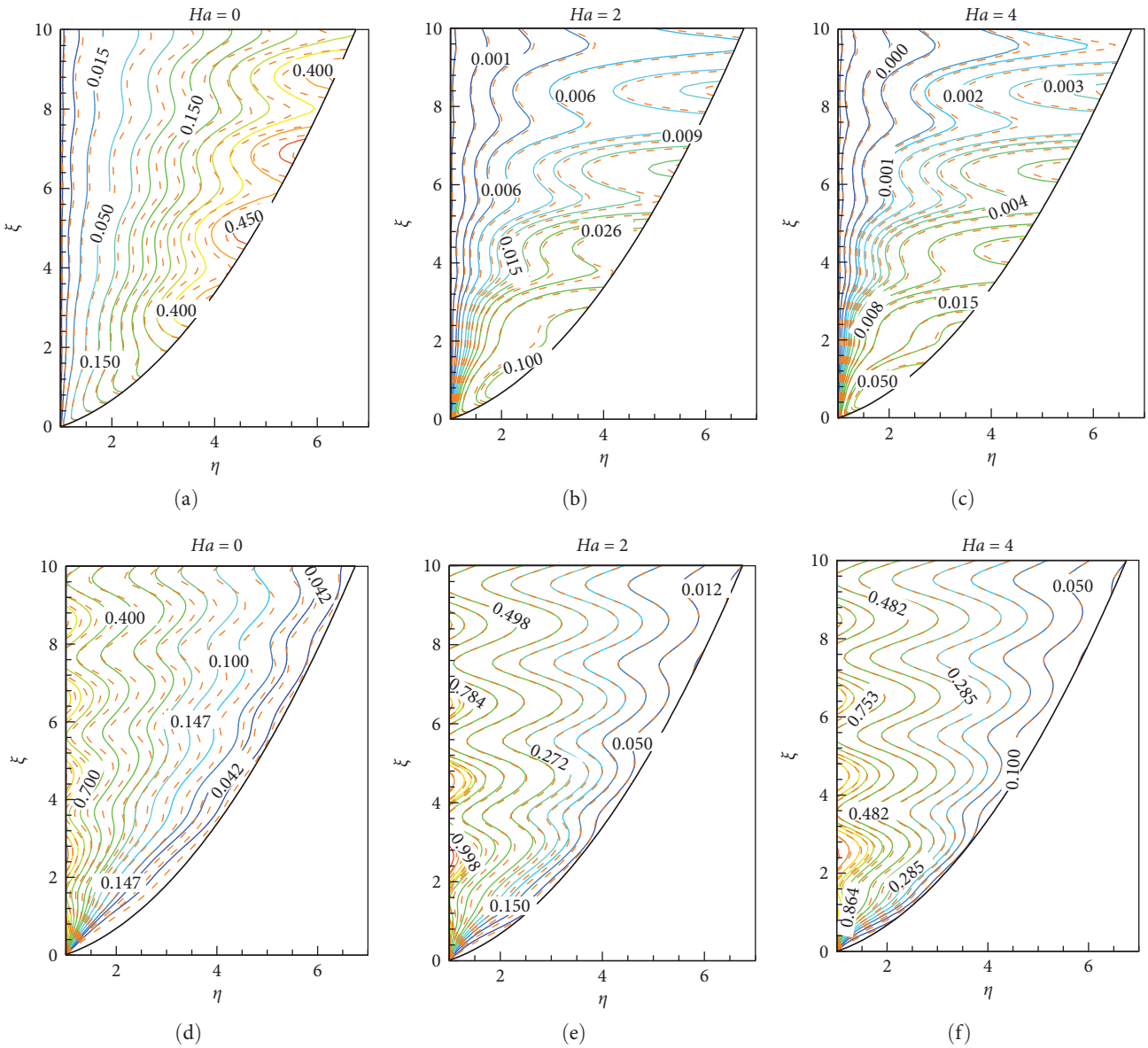

FIGURE 9: Streamlines (top) and isotherms (bottom) for different Hartmann numbers (a), (d) $Ha = 0$; (b), (e) $Ha = 2$; and (c), (f) $Ha = 4$; with volume fraction of $\phi = 0.0$ (solid lines) and $\phi = 0.1$ (dashed lines), while $\varepsilon = 0.3$ with $Pr = 6.2$.

In Figure 11, the volume fraction ($\phi = 0.0$, $\phi = 0.02$, $\phi = 0.05$, $\phi = 0.08$, and $\phi = 0.1$) for skin friction and Nusselt number varies. For higher values, the increases and approaches its maximum value at the upper part of the cylinder as the fluid motion is clockwise. It is shown that the velocity distribution of nanofluid increases with volume fractions near the left wall, as predicted by a thin layer of hydrodynamic velocity boundary layers. Nanoparticles accelerate the flow phenomenon; as a result, the heat transfer process also increases. Higher velocity and temperature lead to lower skin friction and a higher rate of heat transfer. According to Figure 11(a), the skin friction decreases when nanoparticles are included. This is because the presence of the nanoparticles causes the fluid to thicken and become more challenging to move. The Nusselt number, which has no measurements, determines how much heat is transmitted across a surface via convection instead of conduction. By incorporating nanoparticles into a stream, one can increase the Nusselt number by enhancing convective heat transfer. This is because the nano-materials can increase the fluid's thermal conductivity, increasing convective heat transfer. As a result, in Figure 11(b) it is seen that the Nusselt number increases as well. In conclusion, we can say that improved heat transfer reduces the skin friction.

Figure 12 shows the effect of ε and ϕ on the heat transfer rate Nu. The heat transfer has been plotted for different ε for different ϕ. Due to the unique thermal characteristics of hybrid nanofluids, the effectiveness of heat transfer improves. The thermophysical characteristics of the base fluid are enhanced by the inclusion of nanoparticles. The existence of hybrid nanofluids can affect the heat transfer properties in a situation of natural convection over a thin vertical cylinder. Hybrid nanofluids' improved thermal conductivity can facilitate heat transfer by

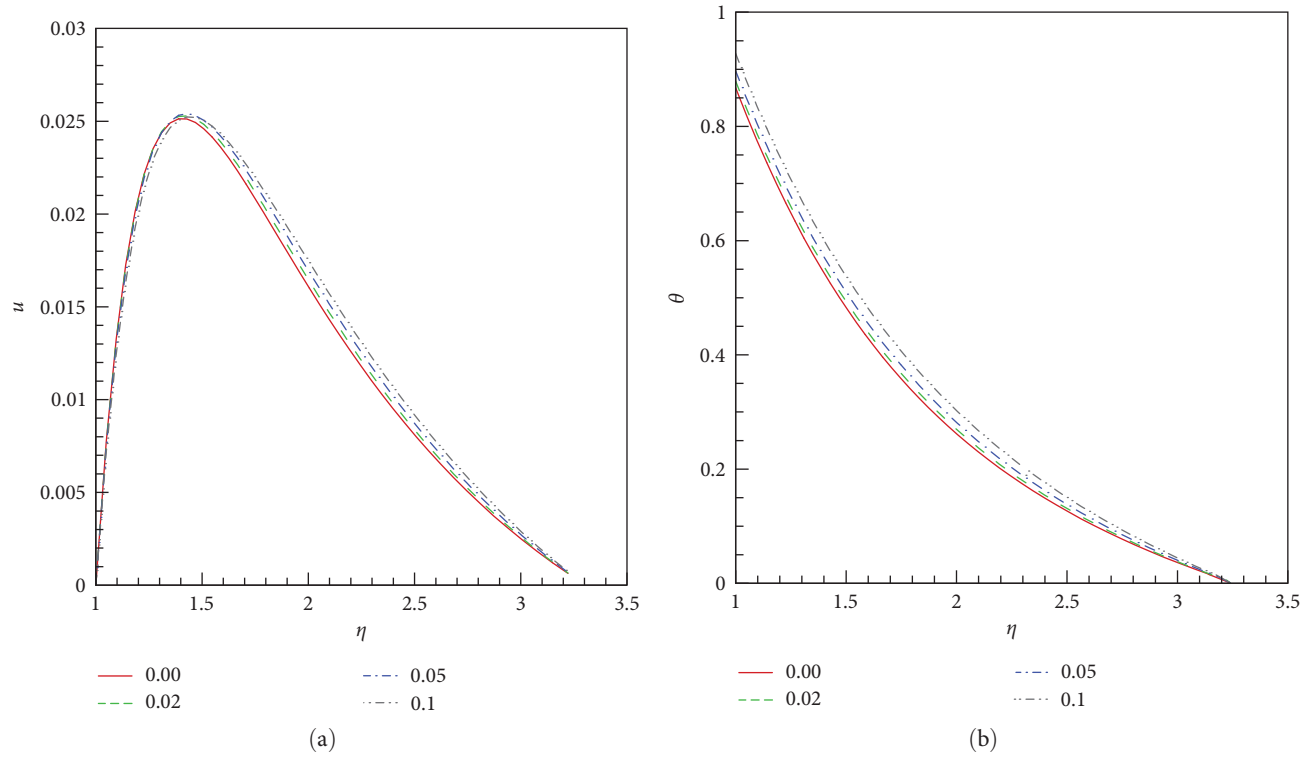

FIGURE 10: (a) Velocity and (b) temperature with different volume fractions, ϕ while $\varepsilon = 0.3$ with $Pr = 6.2$ at $\xi = 2$.

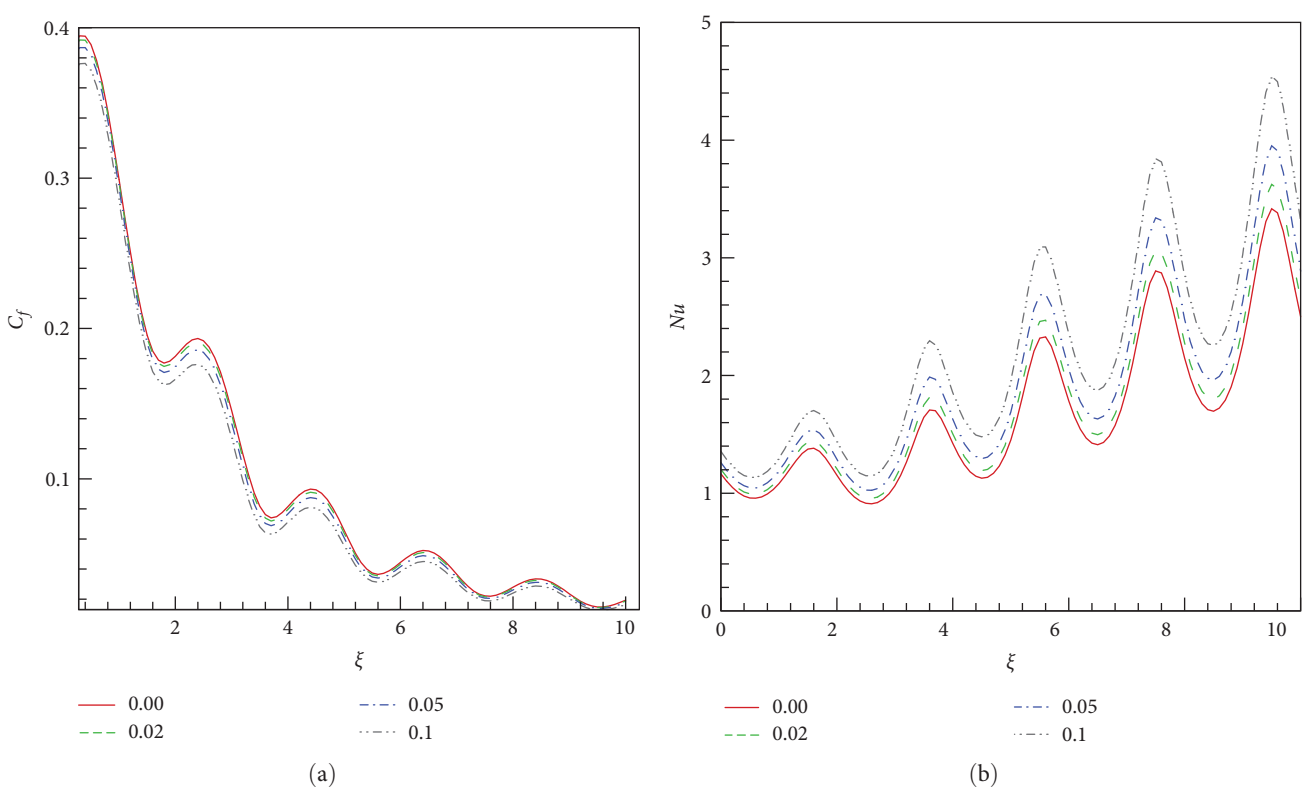

FIGURE 11: (a) Skin friction and (b) Nusselt number with different volume fractions, for $\phi = 0.0$, $\phi = 0.02$, $\phi = 0.05$, and $\phi = 0.1$; while $\varepsilon = 0.3$ with $Pr = 6.2$.

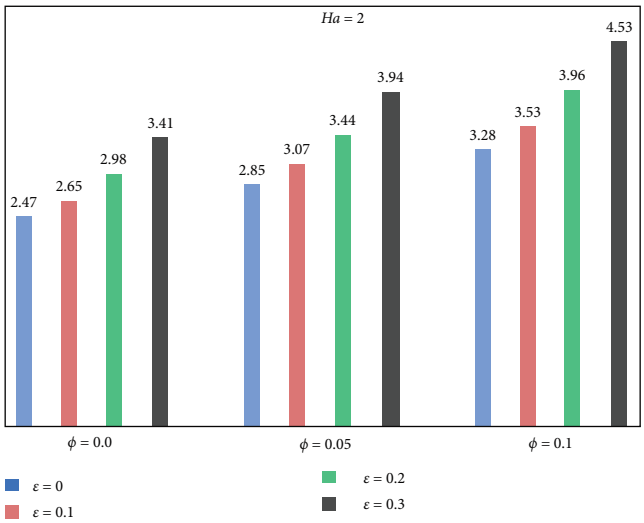

FIGURE 12: Maximum heat transfer rate at various ϕ (0, 0.05, 0.1) and ε (0, 0.1, 0.2, 0.3), while $Ha = 2$.

enhancing fluid conduction. A greater Nusselt number results from this improved heat conductivity. The figure shows that Nu increases by 24.72% as ϕ increases from 0 to 0.1 while $\varepsilon = 0.3$. From Figure 12, it is also seen that the convective heat transmission between the fluid and the surface can rise if the temperature fluctuation's amplitude increases. Data show that Nu increases 27.66% while ε increases from 0.0 to 0.3 at 5% hybrid nanoparticles. This is due to the temperature changes resulting in improved heat transmission. That is why the Nu can increase with an increase in the ε.

7. Conclusions

In the present article, a numerical analysis of MHD natural convection in a thin vertical cylinder with a uniform wall heat flux condition filled with copper (Cu) and aluminum-oxide (Al_2O_3), which are hybrid nanofluids, has been studied here. Numerical simulations have been performed for a wide range of governing parameters: Hartmann number from $Ha = 0$ to $Ha = 4$, nanoparticle volume fraction $\phi = 0.0$, $\phi = 0.05$, $\phi = 0.1$; amplitude $\varepsilon = 0.0$–$\varepsilon = 0.3$ and Prandtl number, $Pr = 6.2$. The effects of different physical factors on heat transfer and fluid flow have been demonstrated in terms of streamlines and isotherms, skin friction and Nusselt number, as well as velocity and temperature distribution. The following outcomes of the results are summarized below:

(i) The heat transfer rate in terms of Nusselt number and skin friction increased with particle volume fractions.

(ii) It can be seen from the obtained result that amplitude enhances the velocity and temperature distribution along the cylinder.

(iii) The variation of velocity and temperature distribution has shown almost similar trends for all values of particle volume fractions, velocity, and temperature increases with the effect of hybrid nanofluids.

(iv) Skin friction slightly decreases as the effect of hybrid nanofluid increases, while Nu increases with nanoparticle volume fractions. That means improved heat transfer reduces the skin friction.

(v) It shows that the magnitude of the streamline and isotherm increases with the amplitude increase, and for different amplitudes, the isotherm varies; that is, the waves increase as we increase the amplitudes from 0.0 to 0.3.

(vi) The maximum Nu number has been found at the maximum amplitude (ε) with maximum ϕ. Nu number retards the fluid flow; hence, Nu number decreases as Ha increases.

(vii) Nu increases 24.72% as ϕ increases from 0 to 0.1 while $\varepsilon = 0.3$, and 27.66% while ε increases from 0.0 to 0.3 at 5% hybrid nanoparticles.

(viii) The velocity and magnitude of the streamline and isotherm also decrease as the Ha number increases. On the other hand, temperature increases as Ha number increases.

(ix) Hybrid nanoparticles increase the thermal conductivity of the fluid; as a result, the heat transfer rate increases in all cases with the effect ϕ.

Nomenclature

English Symbols

A: Area of the cylinder
Al_2O_3: Aluminum oxide (commonly called as "Alu-mina")
B_o: Magnetic force kg $s^{-1}A^{-1}$
Cu: Copper
C_p: Specific heat J $kg^{-1}K^{-1}$
g: Gravitational acceleration ms^{-2}
Gr: Grashof number
Ha: Hartmann number
k: Thermal conductivity $Jm^{-1}s^{-1}K^{-1}$
Pr: Prandlt number
q_w: Heat flux of the wall kg s^{-3}
R: Dimensionless radius of the cylinder
r, θ: Cylindrical coordinates
s: Entropy generations $Jm^{-3}s^{-1}K^{-1}$
T: Temperature or wall temperature K
T_∞: Surrounding or ambient temperature K
u, v: Dimensionless velocity coordinates
x, y: Dimensionless Cartesian coordinates

Greek Symbols

α: Thermal diffusivity m^2s^{-1}
β: Thermal expansion coefficient K^{-1}
ϵ: Amplitude
μ: Dynamic viscosity kg $m^{-1}s^{-1}$
η: Coefficient of viscosity N $m^{-2}s$
ρ: Fluid density kg m^{-3}
ν: Kinematic viscosity m^2s^{-1}

σ: Electrical conductivity A m^{-2}
ϕ: Volume fraction
ψ: Dimensionless stream fraction
ξ: Spatial coordinate m

Subscripts

f: Base fluid
np: Nanoparticle
hnf: Hybrid nanofluid
w: Wall of cylinder

Appendix

A. Calculation of Partial Derivatives

To calculate heat transfer in terms of the local and average Nusselt numbers, the equations expressed below, respectively, for natural convection. The calculations for the transformation of heat flux along a thin vertical cylinder are as follows:

$$\begin{aligned} u &= \frac{1}{r}\frac{\partial \psi}{\partial r} \\ &= \frac{1}{r}\frac{\partial}{\partial r}\left[5\nu_f R Gr_x^{1/5} f(\xi,\eta)\right] \\ &= \frac{1}{r}5\nu_f R Gr_x^{1/5}\left[\frac{\partial f}{\partial \xi}\frac{\partial \xi}{\partial r}+\frac{\partial f}{\partial \eta}\frac{\partial \eta}{\partial r}\right] \\ &= \frac{1}{r}5\nu_f R Gr_x^{1/5}\left[\frac{\partial f}{\partial \xi}0+f'\frac{2r}{2Rx}Gr_x^{1/5}\right] \\ &= 5\frac{\nu_f}{r}R Gr_x^{1/5}\frac{r}{Rx}Gr_x^{1/5}f' \\ &= 5\frac{\nu_f}{r}Gr_x^{2/5}f' \end{aligned} \tag{A.1}$$

$$\begin{aligned} v &= -\frac{1}{r}\frac{\partial \psi}{\partial x} \\ &= -\frac{1}{r}\frac{\partial}{\partial x}\left[5\nu_f R Gr_x^{1/5} f(\xi,\eta)\right] \\ &= -\frac{1}{r}5\nu_f R\left[Gr_x^{1/5}\left(\frac{\partial f}{\partial \xi}\frac{\partial \xi}{\partial x}+\frac{\partial f}{\partial \eta}\frac{\partial \eta}{\partial x}\right)+\frac{4}{5}f\frac{g\rho_f q_w x^{1/5}}{5k_f\nu_f^2}\right] \\ &= -\frac{1}{r}5\nu_f R\left[Gr_x^{1/5}\left(\frac{\partial f}{\partial \xi}\frac{1}{5x}\xi-f'\frac{1}{5x}\eta\right)+\frac{4}{5x}fGr_x^{1/5}\right] \\ &= -\frac{1}{r}5\nu_f R Gr_x^{1/5}\frac{1}{5x}\left[\xi\frac{\partial f}{\partial \xi}-\eta f'+4f\right] \\ &= -\left(\frac{R}{r}\right)\frac{\nu_f}{x}Gr_x^{1/5}\left[\xi\frac{\partial f}{\partial \xi}-\eta f'+4f\right] \end{aligned} \tag{A.2}$$

$$\begin{aligned} \frac{\partial u}{\partial x} &= \frac{\partial}{\partial x}\left[5\frac{\nu_f}{r}Gr_x^{2/5}f'\right] \\ &= 5\nu_f\left[\frac{Gr_x^{2/5}}{x}\left(\frac{\partial f'}{\partial \xi}\frac{\partial \xi}{\partial x}+\frac{\partial f'}{\partial \eta}\frac{\partial \eta}{\partial x}\right)+f'\frac{3}{5x}\frac{Gr_x^{2/5}}{x}\right] \\ &= 5\nu_f\frac{Gr_x^{2/5}}{x}\left[\frac{\partial f'}{\partial \xi}\frac{1}{5x}\xi-f''\frac{1}{5x}\eta+\frac{3}{5x}f'\right] \\ &= 5\nu_f\frac{Gr_x^{2/5}}{x}\frac{1}{5x}\left[\xi\frac{\partial f'}{\partial \xi}-\eta f''+3f'\right] \\ &= \frac{\nu_f}{x_2}Gr_x^{2/5}\left[\xi\frac{\partial f'}{\partial \xi}-\eta f''+3f'\right] \end{aligned} \tag{A.3}$$

$$\begin{aligned} \frac{\partial u}{\partial r} &= \frac{\partial}{\partial r}\left[5\frac{\nu_f}{x}Gr_x^{2/5}f'\right] \\ &= 5\frac{\nu_f}{x}Gr_x^{2/5}\left[\frac{\partial f'}{\partial \xi}\frac{\partial \xi}{\partial r}+\frac{\partial f'}{\partial \eta}\frac{\partial \eta}{\partial r}\right] \\ &= 5\frac{\nu_f}{x}Gr_x^{2/5}\left[\frac{\partial f'}{\partial \xi}0+f''\frac{2r}{2Rx}Gr_x^{1/5}\right] \\ &= \left(\frac{r}{R}\right)5\frac{\nu_f}{x^2}Gr_x^{3/5}f'' \end{aligned} \tag{A.4}$$

$$\begin{aligned} \frac{\partial}{\partial r}\left(r\frac{\partial u}{\partial r}\right) &= r\frac{\partial^2 u}{\partial r^2}+\frac{\partial u}{\partial r} \\ &= 5\frac{\nu_f}{x^2}\left(\frac{r}{R}\right)Gr_x^{3/5}\left[r\left(\frac{\partial f''}{\partial \xi}\frac{\partial \xi}{\partial r}+\frac{\partial f''}{\partial \eta}\frac{\partial \eta}{\partial r}\right)+f''\right]+\frac{\partial u}{\partial r} \\ &= 5\frac{\nu_f}{x^2}\left(\frac{r}{R}\right)Gr_x^{3/5}\left[r\left(\frac{\partial f''}{\partial \xi}0+f'''\frac{2r}{2Rx}Gr_x^{1/5}\right)+f''\right]+\frac{\partial u}{\partial r} \\ &= 5\frac{\nu_f}{x^2}\left(\frac{r}{R}\right)Gr_x^{3/5}\frac{r^2}{Rx}Gr_x^{1/5}f'''+5\frac{\nu_f}{x^2}\left(\frac{r}{R}\right)Gr_x^{3/5}f''+5\frac{\nu_f}{x^2}\left(\frac{r}{R}\right)Gr_x^{3/5}f'' \\ &= 5\frac{\nu_f}{x^3}\left(\frac{r^3}{R^2}\right)Gr_x^{4/5}f'''+5\frac{\nu_f}{x^2}\left(\frac{r}{R}\right)Gr_x^{3/5}f''+5\frac{\nu_f}{x^2}\left(\frac{r}{R}\right)Gr_x^{3/5}f''. \end{aligned} \tag{A.5}$$

For temperature:

$$\begin{aligned} \frac{\partial T}{\partial x} &= \frac{\partial}{\partial r}\left[T_\infty+\frac{q_w x}{k_f}Gr_x^{-1/5}\theta\right] \\ &= \frac{q_w}{k_f}\left[\frac{x}{Gr_x^{1/5}}\left(\frac{\partial \theta}{\partial \xi}\frac{\partial \xi}{\partial x}+\frac{\partial \theta}{\partial \eta}\frac{\partial \eta}{\partial x}\right)+\frac{\theta}{5}\frac{x^{-4/5}g\beta_f q_w}{5k_f\nu_f^2}\right] \\ &= \frac{q_w}{k_f}\left[\frac{x}{Gr_x^{1/5}}\left(\frac{\partial \theta}{\partial \xi}\frac{1}{5x}\xi-\theta'\frac{1}{5x}\eta\right)+\theta\frac{1}{5Gr_x^{1/5}}\right] \\ &= \frac{q_w}{k_f}\frac{x}{Gr_x^{1/5}}\left[x\frac{1}{5x}\left(\xi\frac{\partial \theta}{\partial \xi}-\eta\theta'\right)+\theta\frac{1}{5}\right] \\ &= \frac{q_w}{5k_f}\frac{x}{Gr_x^{1/5}}\left[\xi\frac{\partial \theta}{\partial \xi}-\eta\theta'+\theta\right] \end{aligned} \tag{A.6}$$

$$\begin{aligned}\frac{\partial T}{\partial r} &= \frac{\partial}{\partial r}\left[T_\infty + \frac{q_w x}{k_f} Gr_x^{-1/5}\theta\right] \\ &= \frac{q_w x}{k_f} Gr_x^{-1/5}\left[\frac{\partial\theta}{\partial\xi}\frac{\partial\xi}{\partial r} + \frac{\partial\theta}{\partial\eta}\frac{\partial\eta}{\partial r}\right] \\ &= \frac{q_w x}{k_f} Gr_x^{-1/5}\left[\frac{\partial\theta}{\partial\xi}0 + \theta'\frac{2r}{2Rx}Gr_x^{1/5}\right] \\ &= \left(\frac{r}{R}\right)\frac{q_w}{k_f}\theta'\end{aligned} \tag{A.7}$$

$$\begin{aligned}\frac{\partial}{\partial r}\left(r\frac{\partial T}{\partial r}\right) &= r\frac{\partial^2 T}{\partial r^2} + \frac{\partial T}{\partial r} \\ &= r\frac{\partial}{\partial r}\left[\left(\frac{r}{R}\right)\frac{q_w}{k_f}\theta'\right] + \frac{\partial T}{\partial r} \\ &= \left(\frac{r}{R}\right)\frac{q_w}{k_f}\left[r\left(\frac{\partial\theta'}{\partial\xi}\frac{\partial\xi}{\partial r} + \frac{\partial\theta'}{\partial\eta}\frac{\partial\eta}{\partial r}\right) + \theta'\right] + \frac{\partial T}{\partial r} \\ &= \left(\frac{r}{R}\right)\frac{q_w}{k_f}\left[r\left(\frac{\partial\theta'}{\partial\xi}0 + \theta''\frac{2r}{2Rx}Gr_x^{1/5}\right) + \theta'\right] + \frac{\partial T}{\partial r} \\ &= \left(\frac{r^3}{R^2}\right)\frac{q_w}{k_f x}Gr_x^{1/5}\theta'' + \left(\frac{r}{R}\right)\frac{q_w}{k_f}\theta' + \left(\frac{r}{R}\right)\frac{q_w}{k_f}\theta' \\ &= \left(\frac{r^3}{R^2}\right)\frac{q_w}{k_f x}Gr_x^{1/5}\theta'' + 2\left(\frac{r}{R}\right)\frac{q_w}{k_f}\theta'\end{aligned} \tag{A.8}$$

B. Code Implementation Using FORTRAN

Here, we will give some part of the FORTRAN code for the momentum equation as follows:

Here, NX = maximum number x points, N = maximum number y points

```
!=================================================
SW = 0.5
Do II = 2, NX
DO 50 I = 2, N-1
      N1 = (1. + x(ii) *eta(i)) *(viscosity/rho)
      N2 = x(ii)  *(viscosity/rho)
      N3 = beata
      P4 = (Ha *Ha) *sigma/rho
   dvdx = (v(i, 3)-v(i, 1))/DX
   T1 = H/2.0 *(N2 + 4 *V(I, 3) + x(ii) *dvdx)
   A(I) = N1 − T1
   C(I) = N1 + T1
   B(I) = −2.  *N1–3.  *U(I, 3) *H2–N4 *H2-U(I, 3) *H2 *X(II)/DX
50 D(I) = −H2 *(N3 *T(I, 3) + X(II)/DX *U(I, 3) *U(I, 1))
   B(1) = 1.
   C(1) = 0.0
   D(1) = 0.0
   D(N) = 0.0
   BC = 0.0
   CALL THOMSON(0, BC, N, NETA, A, B, C, D)
   DO 60 I = 1, N
60 U(I, 3) = D(I) *(1.0-SW) + SW *U(I, 3)

ENDOO
!=================================================
```

```
!! SUBROUTINE THOMSON(NBC, BC, N, M, A, B, C, D)
! A(I) *W(I − 1) + B(I) *W(I) + C(I) *W(I + 1) = D(I)
! CONSTANT TW NEEDS NBC = 0
! CONSTANT QW NEEDS NBC = 1
   IMPLICIT REAL*8 (A–H, O–Z)
   DIMENSION A(M), B(M), C(M), D(M)
   IF(NBC.NE.0) GO TO 50
      D(1) = BC
      B(N) = 1.0
      D(N) = 0.0
   DO 10 K = 2, N-1
         TEMP = A(K)/B(K − 1)
   B(K) = B(K)-TEMP *C(K − 1)
10 D(K) = D(K)-TEMP *D(K − 1)
   D(N) = D(N)/B(N)
   DO 20 K = 2, N
   KK = N–K + 1
   IF(ABS(B(KK)).LE.1.0E-50) GO TO 50
20 D(KK) = (D(KK)-C(KK) *D(KK + 1))/B(KK)
   RETURN
50 WRITE (6,200) K
200 FORMAT (//' ***BOUNDARY CONDITIONS ARE
INCORRECT ***',1          I6/)
   RETURN
   END
```

Data Availability

This study was not associated with any third-party data.

Conflicts of Interest

The authors declare that they have no conflicts of interest.

Acknowledgments

The first author acknowledges to the North South University (grant no.: CTRG-21-SEPS-09), and the last author acknowledges to the Ministry of Science and Technology (grant no.: EAS/SRG222427) for the financial support.

References

[1] N. Biswas, D. K. Mandal, N. K. Manna, R. S. R. Gorla, and A. J. Chamkha, "Hybridized nanofluidic convection in umbrella-shaped porous thermal systems with identical heating and cooling surfaces," *International Journal of Numerical Methods for Heat & Fluid Flow*, vol. 33, no. 9, pp. 3164–3201, 2023.

[2] D. K. Mandal, N. Biswas, N. K. Manna, R. S. R. Gorla, and A. J. Chamkha, "Magneto-hydrothermal performance of hybrid nanofluid flow through a non-Darcian porous complex wavy enclosure," *The European Physical Journal Special Topics*, vol. 231, no. 13-14, pp. 2695–2712, 2022.

[3] N. Biswas, M. K. Mondal, D. K. Mandal, N. K. Manna, R. S. R. Gorla, and A. J. Chamkha, "A narrative loom of hybrid nanofluid-filled wavy walled tilted porous enclosure imposing a partially active magnetic field," *International Journal of Mechanical Sciences*, vol. 217, Article ID 107028, 2022.

[4] A. Zeeshan, A. Majeed, M. J. Akram, and F. Alzahrani, "Numerical investigation of MHD radiative heat and mass transfer of nanofluid flow towards a vertical wavy surface with viscous dissipation and Joule heating effects using Keller-box method," *Mathematics and Computers in Simulation*, vol. 190, pp. 1080–1109, 2021.

[5] G. Kalpana, K. R. Madhura, and R. B. Kudenatti, "Magnetohydrodynamic boundary layer flow of hybrid nanofluid with the thermophoresis and Brownian motion in an irregular channel: a numerical approach," *Engineering Science and Technology, an International Journal*, vol. 32, Article ID 101075, 2022.

[6] I. Tlili, H. A. Nabwey, M. G. Reddy, N. Sandeep, and M. Pasupula, "Effect of resistive heating on the incessantly poignant thin needle in magnetohydrodynamic Sakiadis hybrid nanofluid," *Ain Shams Engineering Journal*, vol. 12, no. 1, pp. 1025–1032, 2021.

[7] N. S. Khashi'ie, N. M. Arifin, I. Pop, R. Nazar, and E. H. Hafidzuddin, "A new similarity solution with stability analysis for three-dimensional boundary layer of hybrid nanofluids," *International Journal of Numerical Methods for Heat & Fluid Flow*, vol. 31, no. 3, pp. 809–828, 2021.

[8] S. O. Giwa, M. Sharifpur, and J. P. Meyer, "Experimental study of the thermo-convection performance of hybrid nanofluids of Al_2O_3-MWCNT/water in a differentially heated square cavity," *International Journal of Heat and Mass Transfer*, vol. 148, Article ID 119072, 2020.

[9] S. Anitha, K. Loganathan, and M. Pichumani, "Approaches for modelling of industrial energy systems: correlation of heat transfer characteristics between magnetohydrodynamics hybrid nanofluids and performance analysis of industrial length-scale heat exchanger," *Journal of Thermal Analysis and Calorimetry*, vol. 144, pp. 1783–1798, 2021.

[10] B. Venkateswarlu and P. V. Satya Narayana, "Cu-Al_2O_3/H_2O hybrid nanofluid flow past a porous stretching sheet due to temperature-dependent viscosity and viscous dissipation," *Heat Transfer*, vol. 50, no. 1, pp. 432–449, 2021.

[11] R. Pourrajab, I. Ahmadianfar, M. Jamei, and M. Behbahani, "A meticulous intelligent approach to predict thermal conductivity ratio of hybrid nanofluids for heat transfer applications," *Journal of Thermal Analysis and Calorimetry*, vol. 146, no. 2, pp. 611–628, 2021.

[12] U. Yashkun, K. Zaimi, N. A. A. Bakar, I. Pop, and A. Ishak, "MHD hybrid nanofluid flow over a permeable stretching/shrinking sheet with thermal radiation effect," *International Journal of Numerical Methods for Heat & Fluid Flow*, vol. 31, no. 3, pp. 1014–1031, 2020.

[13] F. Gori, M. G. Serranò, and Y. Wang, "Natural convection along a vertical thin cylinder with uniform and constant wall heat flux," *International Journal of Thermophysics*, vol. 27, no. 5, pp. 1527–1538, 2006.

[14] V. Esfahanian and F. Torabi, "Numerical simulation of lead-acid batteries using Keller–Box method," *Journal of Power Sources*, vol. 158, no. 2, pp. 949–952, 2006.

[15] A. Hossain, M. J. Anee, S. Thohura, and M. M. Molla, "Finite difference simulation of free convection of non-Newtonian nanofluids with radiation effects over a truncated wavy cone," *Pramana*, vol. 97, no. 4, Article ID 168, 2023.

[16] V. M. Soundalgekar and P. Ganesan, "Finite-difference analysis of transient free convection with mass transfer on an isothermal vertical flat plate," *International Journal of Engineering Science*, vol. 19, no. 6, pp. 757–770, 1981.

[17] M. M. MacDevette, T. G. Myers, and B. Wetton, "Boundary layer analysis and heat transfer of a nanofluid," *Microfluidics and Nanofluidics*, vol. 17, pp. 401–412, 2014.

[18] M. M. Molla, M. A. Hossain, and M. A. Taher, "Magnetohydrodynamic natural convection flow on a sphere with uniform heat flux in presence of heat generation," *Acta Mechanica*, vol. 186, no. 1–4, pp. 75–86, 2006.

[19] D. K. Mandal, N. Biswas, N. K. Manna, R. S. R. Gorla, and A. J. Chamkha, "Role of surface undulation during mixed bioconvective nanofluid flow in porous media in presence of oxytactic bacteria and magnetic fields," *International Journal of Mechanical Sciences*, vol. 211, Article ID 106778, 2021.

[20] M. A. Hossain, S. C. Paul, and A. C. Mandal, "Natural convection flow along a vertical circular cone with uniform surface temperature and surface heat flux in a thermally stratified medium," *International Journal of Numerical Methods for Heat & Fluid Flow*, vol. 12, no. 3, pp. 290–305, 2002.

[21] M. A. Hossain and M. A. Alim, "Natural convection-radiation interaction on boundary layer flow along a thin vertical cylinder," *Heat and Mass Transfer*, vol. 32, pp. 515–520, 1997.

[22] R. Smith, H. Inomata, and C. Peters, "Heat transfer and finite-difference methods," in *Supercritical Fluid Science and Technology*, vol. 4, pp. 557–615, Elsevier, 2013.

[23] W. J. Minkowycz and E. M. Sparrow, "Local nonsimilar solutions for natural convection on a vertical cylinder," *Journal of Heat Transfer*, vol. 96, no. 2, pp. 178–183, 1974.

[24] K.-T. Yang, "Possible similarity solutions for laminar free convection on vertical plates and cylinders," *Journal of Computational and Applied Mathematics*, vol. 27, no. 2, pp. 230–236, 1960.

[25] S. Ghosh Moulic and L. S. Yao, "Natural convection along a vertical wavy surface with uniform heat flux," *Journal of Heat Transfer*, vol. 111, no. 4, pp. 1106–1108, 1989.

[26] J. J. Heckel, T. S. Chen, and B. F. Armaly, "Natural convection along slender vertical cylinders with variable surface heat flux," *Journal of Heat Transfer*, vol. 111, no. 4, pp. 1108–1111, 1989.

[27] N. Chandra Roy and A. Ghosh, "Magnetohydrodynamic natural convection of second-grade hybrid nanofluid on variable heat flux surface," *AIP Advances*, vol. 12, no. 3, Article ID 035243, 2022.

[28] M. M. Molla, S. C. Saha, and M. A. Hossain, "Radiation effect on free convection laminar flow along a vertical flat plate with streamwise sinusoidal surface temperature," *Mathematical and Computer Modelling*, vol. 53, no. 5-6, pp. 1310–1319, 2011.

[29] A. J. Chamkha, A. M. Rashad, and A. M. Aly, "Transient natural convection flow of a nanofluid over a vertical cylinder," *Meccanica*, vol. 48, no. 1, pp. 71–81, 2013.